Research Square

Preprints are preliminary reports that have not undergone peer review.
They should not be considered conclusive, used to inform clinical practice,
or referenced by the media as validated information.

Decoupled infiltration and isotope signals reveal hidden East Asian monsoon megadroughts

Adam Hartland

adam.hartland@lincoln.ac.nz

Lincoln University

Bedartha Goswami

IISER Pune

Sebastian Höpker

University of Waikato

Jungho Park

Lincoln Agritech Ltd

Dorisel Torres-rojas

University of Waikato

Jin Liao

Wuhan Geological Survey Center of China Geological Survey

Bethany Fox

University of Salford

Norbert Marwan

Potsdam Institute for Climate Impact Research https://orcid.org/0000-0003-1437-7039

Sebastian Breitenbach

Northumbria University https://orcid.org/0000-0001-9615-2065

Chaoyong Hu

State Key Laboratory of Biogeology and Environmental Geology of Ministry of Education , China University of Geosciences

Article

Keywords:

Posted Date: June 1st, 2026

DOI: https://doi.org/10.21203/rs.3.rs-9366721/v1

License: This work is licensed under a Creative Commons Attribution 4.0 International License.
Read Full License

Additional Declarations: There is **NO** Competing Interest.

Decoupled infiltration and isotope signals reveal hidden East Asian monsoon megadroughts

Adam Hartland[1–3,*], Bedartha Goswami[4,5], Sebastian Höpker[3], Jungho Park[2], Dorisel Torres Rojas[2,6], Jin Liao[7], Bethany R.S. Fox[8], Norbert Marwan[4], Sebastian F.M. Breitenbach[9], Chaoyong Hu[7]

*[1]Lincoln University, Lincoln 7647, Aotearoa New Zealand. [2]Lincoln Agritech Ltd, Ruakura, Hamilton 3214, Aotearoa New Zealand. [3]Te Aka Mātuatua — School of Science, University of Waikato, Hamilton, Aotearoa New Zealand. [4]Potsdam Institute for Climate Impact Research, Potsdam, Germany. [5]Indian Institute of Science Education and Research, Pune, India. [6]Riddet Institute, Massey University, Palmerston North, Aotearoa New Zealand. [7]China University of Geosciences, Wuhan, China. [8]School of Science, Engineering & Environment, University of Salford, UK. [9]School of Geography and Natural Sciences, Northumbria University, Newcastle upon Tyne, UK. *Correspondence: adam.hartland@lincoln.ac.nz*

Abstract (190 words)

Speleothem $\delta^{18}O$ and prior carbonate precipitation (PCP) proxies conflate East Asian Summer Monsoon (EASM) rainfall with seasonal and karst-hydrological signals, precluding quantitative precipitation estimates. Here we introduce a kinetic proxy that exploits the dissociation of organic-metal complexes in dripwater to reconstruct past drip rates — and, through calibrated regressions, absolute annual precipitation — from stalagmite cobalt (Co) and nickel (Ni). Applied to stalagmite HS4 from Heshang Cave, central China, with Monte Carlo uncertainty propagation, our reconstruction reveals peak Holocene rainfall of ~1,500 mm yr^{-1} in the early Holocene, declining ~33% to ~1,000 mm yr^{-1} by the late Holocene in step with 30°N June insolation. A sharply defined aridity pulse at 5.2 ka coincides with termination of the North African Humid Period, while the absence of a drip-rate reduction at 8.2 ka — despite co-located $\delta^{18}O$ and PCP anomalies — implicates enhanced cave ventilation and winter recharge rather than summer rainfall reduction. A two-phase post-1750 signal reveals Little Ice Age drought recovery followed by progressive equilibration toward modern infiltration rates, recording site-scale dynamics independent of $\delta^{18}O$. The approach yields uncertainty-bounded, unit-bearing infiltration estimates transferable across speleothem archives, opening the way to quantitative Holocene hydroclimate reconstructions.

Main text (~2700 words)

Introduction

The East Asian Summer Monsoon (EASM) sustains nearly two billion people[1], underpinning agriculture and freshwater security across one of the world's most densely populated regions. Yet quantifying its Holocene variability — shaped by orbital[2,3], volcanic[4], and increasingly anthropogenic forcings[5] — remains difficult because the proxies most widely available from speleothem archives do not record rainfall directly[6]. Instrumental observations link EASM variability to El Niño–Southern Oscillation and Indian Ocean Dipole modes[7,8], but such records span only decades, too short to separate natural multi-centennial swings from anthropogenic trends. Stalagmites provide precisely dated, millennial-scale archives[2,9], and geochemical proxies extracted from them — principally $\delta^{18}O$ — have illuminated broad orbital-scale monsoon behaviour. However, $\delta^{18}O$ integrates rainfall amount, moisture source, temperature, seasonality, and atmospheric circulation, generating interpretive ambiguities[10,11]: Holocene trends in Chinese cave records may reflect upstream rainout[10] or cave-ventilation effects rather than changes in monsoon intensity[12]. Prior calcite precipitation (PCP) — inferred from Mg/Ca ratios or $\delta^{45}Ca$[13] — can indicate aquifer drying[6], but translates only indirectly to rainfall, and is itself susceptible to ventilation and degassing biases[14]. These limitations underscore a pressing need for proxies that record local hydrology directly and yield quantitative precipitation estimates with propagated uncertainties.

To address this, we introduce a kinetic proxy that directly encodes local drip-rate history in the trace metal chemistry of stalagmites. Cobalt and nickel in dripwater bind to dissolved organic

matter as OMCs[15,16] characterised by log-normally distributed dissociation rates[15]. Drip rate governs the residence time of the water film on the stalagmite surface, setting the kinetic window available for OMC dissociation and hence the fraction of labile metal available for incorporation into the carbonate[15,17] (Fig. 1). Slow drips allow extensive dissociation and yield elevated solid-phase concentrations; rapid drips truncate the kinetic window and suppress incorporation. By modelling this process with log-normal rate distributions[15], Co and Ni records can be inverted for past drip rate, and — through empirical calibration against monitored cave and meteorological data — for absolute precipitation.

We apply this framework to stalagmite HS4 from Heshang Cave, central China (N30°27′, E110°25′), a well-monitored site on the EASM fringe[18,19] (Fig. 2). Modern monitoring links HS4 drip rates to annual precipitation-to-temperature (P/T) ratios[18]; integrating palaeotemperature from bacterial fatty acids preserved in the same stalagmite[20] and propagating uncertainties through a Bayesian inversion framework[21], we obtain quantitative Holocene precipitation in mm yr^{-1}. The resulting record quantifies orbital-scale trends[2,3,22], resolves abrupt events[23–25], contextualises recent anthropogenic change[5], and settles ongoing proxy debates[12,13,19]. The method is generalisable: any speleothem from a limestone cave hosting Co- or Ni-bearing dripwater is a potential quantitative rainfall archive, and the underlying OMC dissociation framework extends in principle to subaqueous carbonates and other mineral archives (see Discussion).

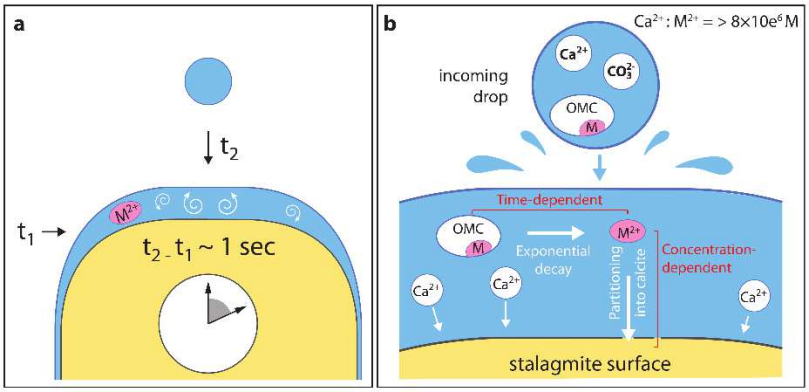


Figure 1 | Conceptual model. (a) The drip interval acts as a kinetic window for OMC dissociation: thin-film residence time (τ) increases as an inverse function of drip rate, following τ = 60/*d* (s), where *d* is drips min^{-1}. (b) Competing thin-film processes governing signal transfer to the stalagmite. Adsorption and partitioning are rapid; OMC dissociation is comparatively slow, throttling labile Co and Ni availability and generating an inverse relationship between drip rate and trace metal concentration.

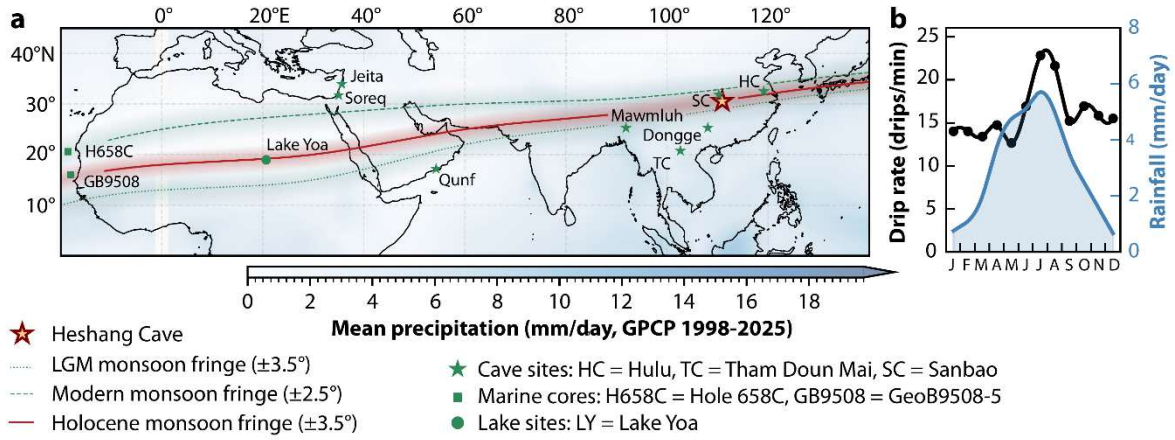


Figure 2 | Site location and modern calibration. (a) Map of mean precipitation (mm day⁻¹; GPCP v2.3, January 1998–July 2025; contours) overlaid on topography and shaded relief. Modern (red, ±2.5° latitude band), Holocene (green dashed, ±3.5°), and LGM (green dotted, ±3.5°) monsoon fringes interpolated from literature syntheses. Heshang Cave (maroon star) and regional proxy sites are marked. (b) Median monthly drip rate at HS4 (black; drips min⁻¹; 2005–2015 monitoring) and median monthly precipitation at the nearest GPCP grid point (30.45°N, 110.417°E; blue; mm day⁻¹; 1998–2025). Curves are cubic spline interpolations.

Results

Kinetic Proxy Framework

In Heshang Cave dripwater, Co and Ni form OMCs[15,16] whose dissociation rate constants (k_d) follow a log-normal distribution[15]. The residence time of the water film, $\tau = 60/d$ (s), sets the extent to which these complexes dissociate before each subsequent drip: labile metal concentrations thus rise monotonically with τ through first-order kinetics[15,17] (Fig. 3). For a single k_d, the labile aqueous concentration $[X]_{aq}^{la}$ is given by:

$$[X]_{aq}^{la} = [(1 - \lambda_F - \lambda_I)(k_d\tau) + \lambda_F][X]_{aq}^{tot} \quad (1)$$

where λ_F is the fast-dissociating fraction (~0.001)[16], λ_I is the inert fraction (~0.10 for Ni, ~0.4 for Co)[15], and $[X]_{aq}^{tot}$ is the total aqueous metal concentration. Extending to a distribution of rates $f(\ln k_d)$ with mean μ and standard deviation σ:

$$[X]_{aq}^{la} = [X]_{aq}^{tot}\left[\lambda_F + (1 - \lambda_F - \lambda_I)\int f(\ln k_d)(k_d\tau)\, d\ln k_d\right] \quad (2)$$

Labile metals partition into calcite with coefficient K_p[17,26]. Because the solid-phase calcium concentration $[Ca_s] \approx 1$ (mole fraction in the calcite matrix), the stalagmite metal concentration $[X_s]$ simplifies to:

$$K_p = \frac{[X]_s/[Ca]_s}{[X]_{aq}^{la}/[Ca]_{aq}} \quad (3)$$

$$[X]_s = K_p\frac{[X]_{aq}^{tot}}{[Ca]_{aq}}\left[\lambda_F + (1 - \lambda_F - \lambda_I)\int f(\ln k_d)(k_d\tau)\, d\ln k_d\right] \quad (4)$$

The resulting forward model shows peak sensitivity below ~15 drips min⁻¹ (Fig. 3), spanning the range typical of palaeoclimate-relevant cave sites. Inversion via the BayProX Bayesian

framework[21] yields posterior probability distributions for drip rate, $p(\tau \mid t)$, from the measured trace metal record (Supplementary Methods 1–2). The inverse relationship is mechanistic and thermodynamically grounded — independent of site-specific empirical tuning of the response function, relying only on independently measured partition coefficients and OMC dissociation parameters.

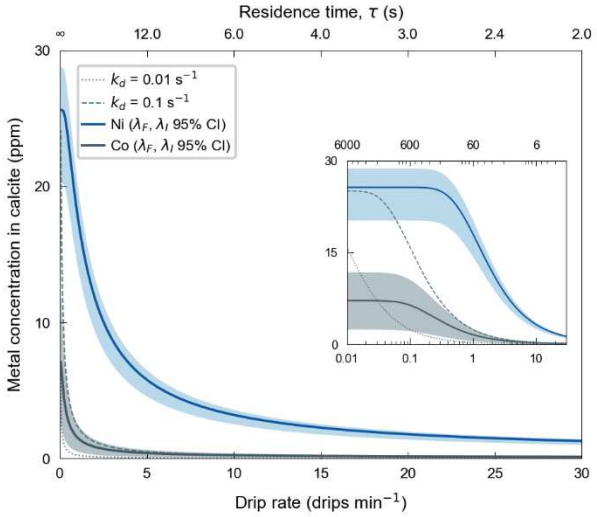


Figure 3 | Forward model sensitivity. Modelled calcite concentrations for log-normal OMC dissociation rate distributions (k_d) with μNi = −3.91 and μCo = −5.57 (σ = 0.22 shown for illustrative clarity; full σ = 1.39 used in inversions). Ni (blue) and Co (grey) curves incorporate λ_F = 0.001 and inert fractions λ_I = 0.10 ± 0.10 (Ni) and 0.40 ± 0.20 (Co)[15]. Shaded areas are 95% confidence intervals from Monte Carlo simulation. Dashed and dotted lines are theoretical end-members for fully labile complexes at fixed k_d = 0.01 s^{-1} and 0.1 s^{-1}. Inset: log-scale drip rate axis with secondary residence time axis (τ, s).

Calibration and Modern Validation

Heshang Cave exhibits a clear hydrographic response to summer monsoonal recharge[18], with HS4 drip rates tracking the seasonal cycle (Fig. 2b). Monitoring data from 2005–2015 reveal a strong positive correlation between annual drip rate and P/T ratio[18] (Fig. 4a). Optimising dissociation rate parameters (μ, σ) against historical Yichang P/T records (1950–2001) through least-squares fitting of 10-yr moving averages, we recover ln k_d distributions closely consistent with independent laboratory determinations from New Zealand cave systems[15] — a cross-hemispheric agreement implying that OMC kinetics are a property of DOM–metal geochemistry rather than a site-specific artefact, supporting broad applicability. Reconstructed drip rates reproduce the observed HS4 baseflow (~17 drips min^{-1}) and the temporal trajectory of P/T through the calibration interval (Fig. 4c).

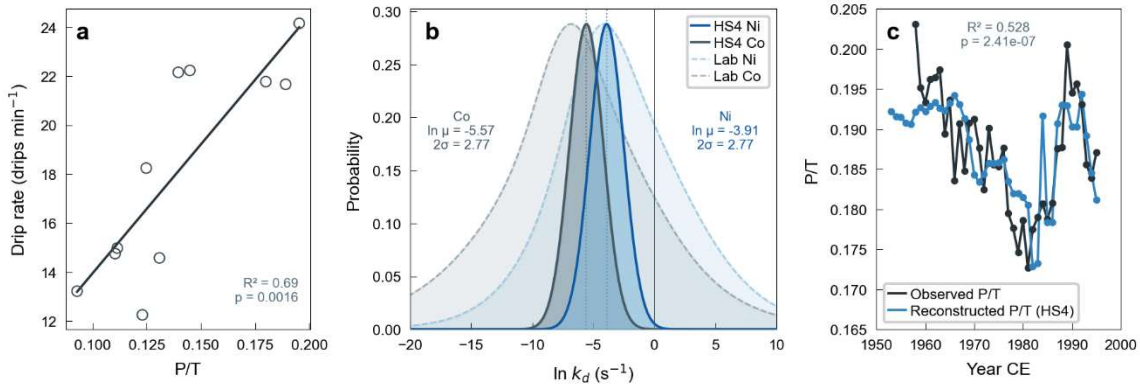


Figure 4 | Calibration progression. (a) Annual P/T ratio versus drip rate (2005–2015 monitoring), with regression fit. (b) Optimised ln k_d distributions for Ni (red) and Co (grey); laboratory-determined values shown as dashed lines[15]. (c) Observed Yichang P/T (black) versus reconstructed (green) over the calibration interval from HS4 Ni and Co.

Holocene Precipitation Reconstruction

Co- and Ni-derived drip rates for stalagmite HS4 declined from a median of ~25 drips min^{-1} at 9.5 ka to ~6 drips min^{-1} in the pre-industrial late Holocene, mirroring the 30°N June insolation trajectory and broadly consistent with the HS4 $\delta^{18}O$ record[19] (Fig. 5; Extended Data Fig. 1). Translating drip rates to absolute precipitation via the chained regression P = (P/T)Yichang × T × 365.25, with Monte Carlo propagation of all parameter uncertainties, early Holocene rainfall peaked at ~1500 mm yr^{-1} (25th–75th percentile range: 1100–2000 mm yr^{-1}), declining ~33% to ~1,000 mm yr^{-1} (700–1,500 mm yr^{-1}) by the late Holocene. This millennial-scale drying tracks the southward migration of the intertropical convergence zone (ITCZ) and progressive weakening of the EASM under declining 30°N June insolation, with reconstructed precipitation showing a robust positive correlation with the Berger & Loutre[2,22] insolation curve (r = 0.80, p < 0.01).

Against this orbital background, the native-resolution reconstruction reveals an abrupt recharge collapse at ~5.2 ka. Over an ~80-year interval, median drip rates fell from ~20 drips min^{-1} to ~1.7 drips min^{-1} — a >90% reduction in inferred cave recharge — with the posterior probability density narrowing to a tight cluster near zero (Fig. 5a; Extended Data Fig. 3B). The co-located $\delta^{18}O$ record shows no excursion during this interval, and Z-score agreement analysis confirms this as the sharpest instantaneous proxy disagreement in the Holocene record (Fig. 5b; Extended Data Fig. 3B). The event aligns temporally with the termination of the North African Humid Period[23,25] and megadroughts reconstructed across mainland Southeast Asia[24], implicating a contracted ITCZ and weakened Walker circulation[25], potentially amplified by a contemporaneous solar minimum[27] and enhanced stratospheric aerosol loading from explosive volcanism[4]. Recurrence quantification analysis (RQA)[28] independently confirms this transition as a dynamical singularity: a prominent positive transitivity excursion in the drip rate series is absent from the $\delta^{18}O$ record (Extended Data Fig. 2; see Discussion).

In marked contrast, the record shows elevated drip rates through the 8.2 ka interval but no evidence of drought. On the best-estimate chronology, a local flanking-baseline test comparing the event core (8.25–8.10 ka; n = 6, median = 20.67 drips min^{-1}) against combined pre- and post-event flanks (n = 21, median = 21.10 drips min^{-1}) yields a non-significant difference (−2.1%, Mann–Whitney U p = 0.59; Extended Data Fig. 4). The broader 8.5–8.0 ka window sits above the early-Holocene baseline (9.0–8.5 ka), driven by the secular insolation trend rather than an event-specific anomaly. This positive drip-rate trajectory stands in apparent tension with the PCP and $\delta^{18}O$ anomalies reported from the same stalagmite[12,13], which record a drying signal, whereas the drip rate reconstruction implies that effective recharge was not reduced (see Discussion).

The best-estimate reconstruction (Fig. 5a; Extended Data Fig. 3) reveals additional structure in the recent record: a sustained drought immediately preceding the post-1800 surge, with drip rates falling to ~4.5 drips min^{-1} (~1737 CE) — a 72% reduction from the late-Holocene baseline — sustained for approximately 60 years. The timing coincides with severe Qing dynasty droughts documented across central China during the 1720–1740 period[29], and with the extreme 1784–1787 drought that affected Hubei and the middle Yangtze[30]. The abruptness of the subsequent transition — from near-cessation of drip flow to the highest sustained drip rates in the Holocene record within a single sampling interval — is consistent with flashy, unbuffered flow through a drained epikarst during recovery from the LIA drought (see Discussion), and underscores the value of the kinetic proxy in resolving centennial-scale variability that age-model smoothing otherwise attenuates (Supplementary Methods 7, S7.7).

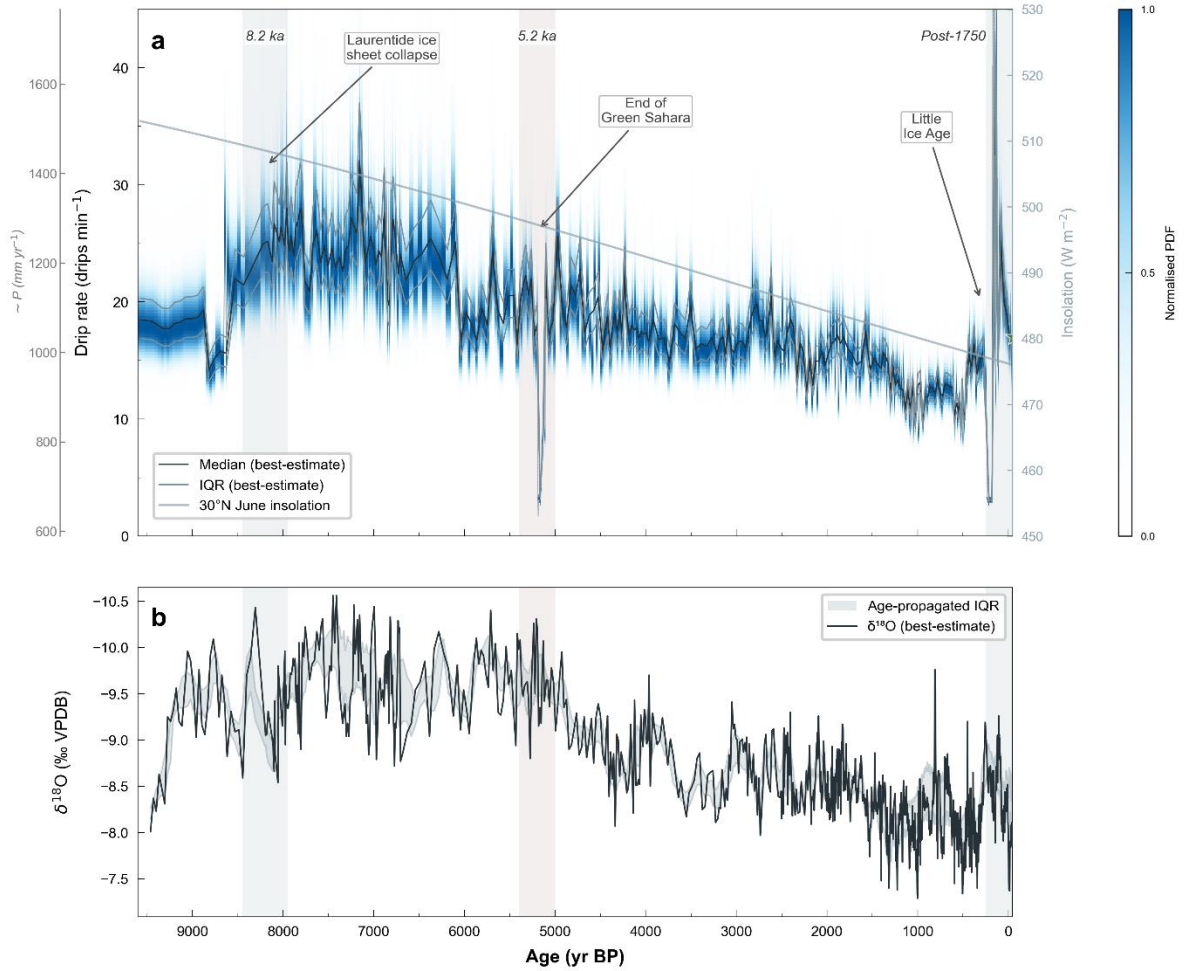


Figure 5 | Holocene drip rate reconstruction and proxy comparison from stalagmite HS4, Heshang Cave. **(a)** Kinetic proxy drip rate reconstruction on the best-estimate chronology. Probability density shading (colourbar: normalised posterior PDF) is shown at native BayProX resolution (~576 points). Median and 25th–75th percentile lines are overlaid at both native resolution (faint, dashed IQR) and 1-cm-smoothed resolution (solid; ~258 points), illustrating high-frequency epikarst variability superimposed on the smoother signal backbone. The age-propagated 25th–75th percentile envelope (pale grey fill; n = 1,000 age-model realisations) shows how chronological uncertainty attenuates abrupt events. Green star marks the calibrated modern baseflow (~17 drips min^{-1}; 2005–2015 monitoring). The 30°N June insolation curve[22] (grey; right axis, W m^{-2}) is overlaid. An approximate precipitation scale (left axis, mm yr^{-1}) is derived from the drip rate–precipitation transfer function (Supplementary Table S2). Shaded vertical bands mark the 8.2 ka event, the ~5.2 ka event, and the post-1750 CE interval; annotated labels indicate the Laurentide ice-sheet collapse, the end of the Green Sahara, and the Little Ice Age. **(b)** Co-located $\delta^{18}O$ record[31] on the best-estimate chronology (dark line), with age-propagated 25th–75th percentile envelope. Event bands are carried through from panel a.

Discussion

The kinetic proxy framework presented here delivers the first speleothem-based precipitation reconstruction in absolute units (mm yr^{-1}), grounded in a mechanistic model of OMC dissociation calibrated against a decade of cave monitoring and regional meteorological data. The Holocene record from HS4 illustrates three distinct modes of EASM behaviour — orbital forcing, abrupt teleconnection events, and centennial-scale infiltration recovery — that the proxy resolves independently and quantitatively.

The millennial-scale decline in precipitation from early to late Holocene is strongly coupled to 30°N June insolation (r = 0.80, p < 0.01; Fig. 6a), reflecting the canonical ITCZ-driven response of the EASM to precessional forcing[32]. The $\delta^{18}O$ record from the same stalagmite shows a weaker and negative correlation with insolation (r = −0.18)[31], likely because $\delta^{18}O$ integrates upstream rainout and vegetation feedbacks[33] that attenuate the local hydrological signal. The kinetic proxy, responding directly to site-scale infiltration, is free of these integrative biases.

The 5.2 ka event emerges as effective EASM failure at the cave site: a near-complete cessation of infiltration sustained for ~80 years, invisible to both $\delta^{18}O$ and $\delta^{13}C$. On the best-estimate chronology, drip rates collapse to ~1.7 drips min^{-1}, reaching >90% below mid-Holocene recharge levels in the native-resolution reconstruction (~84% in the 1-cm-smoothed series) (Fig. 5a; Extended Data Fig. 3b). An independent quantitative precipitation reconstruction from Angulinao Lake on the EASM margin also identifies a 5.2 ka precipitation minimum[34], corroborating the signal. A contemporaneous ~5.18 ka $\delta^{18}O$ excursion at Magou Cave[35] provides independent isotopic corroboration from a separate cave system. Its synchrony with the termination of the North African Humid Period[23,25] and Southeast Asian megadroughts[24] is consistent with a reorganisation of tropical atmospheric circulation during the North African monsoon collapse — a contraction of the Hadley cell and Walker circulation that propagated drought conditions across Afro-Asian monsoon margins[25], likely intensified by a contemporaneous solar minimum[27] and stratospheric aerosol forcing from explosive volcanism[4]. Crucially, the $\delta^{13}C$ record shows negligible change during the event (+0.08 ‰ relative to flanking intervals — well within analytical uncertainty), ruling out vegetation dieback or a C3-to-C4 shift as an amplifying mechanism at Heshang, and further implying negligible PCP influence on $\delta^{13}C$[31] during the event (which would otherwise produce a multi-permil excursion). The overlying subtropical C3 forest evidently survived the recharge collapse, implying that the event represents an infiltration-excess drought — precipitation declined below the threshold for epikarst percolation while remaining above the threshold for vegetation survival. The kinetic proxy thus records the residual moisture flux that passes through the soil–plant system, a hydrological component invisible to both $\delta^{18}O$ (which integrates moisture-source fractionation) and $\delta^{13}C$ (which responds to soil biological activity and PCP). The RQA transitivity signal corroborates this interpretation: the drip rate series shows a sharp positive TRANS excursion at 5.2 ka — indicating the proxy system transiently occupied a more restricted, geometrically clustered region of phase space during peak aridity — while the $\delta^{18}O$ record shows no comparable dynamical response. That DET remains high and stable in both proxies throughout confirms that the 5.2 ka event represents a genuine hydrological excursion within a persistently forced, orbitally structured system, rather than noise or geochemical artefact.

The absence of a drip-rate reduction at 8.2 ka — despite significant PCP and $\delta^{44}Ca$ anomalies in the same stalagmite — has direct implications for the interpretation of traditional speleothem proxies from Heshang Cave. Liu et al.[12] and Owen et al.[13] interpreted these geochemical signals as EASM rainfall reduction linked to the Laurentide meltwater pulse and associated AMOC slowdown[37]. Our reconstruction shows that effective recharge was not reduced during this interval (local flanking test: −2.1%, p = 0.59), implying instead that ventilation-driven CO_2 degassing and a shift in recharge seasonality[10,11,14] affected isotopic and PCP signals while net infiltration was maintained or slightly enhanced, potentially through increased winter precipitation. The +1.1 ‰ $\delta^{13}C$ excursion during the event — the largest in the mid-Holocene portion of the record — independently supports enhanced degassing and PCP rather than a change in overlying vegetation or soil productivity, providing a parsimonious alternative to the drought interpretation. This finding aligns with the global pattern of Parker & Harrison[38], where speleothem responses at 8.2 ka are inconsistent in sign and magnitude across sites, arguing against simple rainfall interpretations for many records.

The recent portion of the HS4 record reveals a two-phase hydrological history that must be interpreted with care. The 18th century drought (~4.5 drips min^{-1} at ~1737 CE; ~823 mm yr^{-1}) represents the driest conditions in the late Holocene, sustained for ~60 years (Fig. 5a; Extended Data Fig. 3c). Following this prolonged drought, drip rates surged abruptly from ~1760 CE, reaching extreme and highly variable values (median 22.9 drips min^{-1}; range 3.2–50.9) during the interval 1760–1850 CE. However, after decades of near-zero recharge, the fully drained epikarst would transmit recovered rainfall as flashy, unbuffered flow that overshoots the equilibrium drip-rate–rainfall relationship. We therefore interpret the 1760–1850 surge primarily as natural recovery from the LIA drought, amplified by epikarst recharge dynamics, rather than as evidence for anthropogenic EASM intensification at that time — atmospheric CO_2 remained near 280 ppm throughout this interval. From ~1850 onwards, drip rates show a progressive decline (−0.06 drips min^{-1} yr^{-1}, r^2 = 0.62) that converges on the modern monitored baseflow (~17 drips min^{-1}) by the mid-20th century. This trajectory is most parsimoniously interpreted as continued epikarst equilibration — the gradual dampening of the transient recharge overshoot as storage refills and the system returns to quasi-steady-state hydrology. Aerosol-driven suppression of the EASM, documented in satellite-era observations[5,39] and large-ensemble model simulations[40], may contribute to the latter portion of this decline (post-1950), but the proxy's multi-decadal sampling resolution cannot separate anthropogenic aerosol effects from the natural recovery signal. CMIP6 projections under 1.5–2°C warming scenarios anticipate 5–18% further increases in EASM precipitation relative to late-20th-century baselines[41] as aerosol emissions decline; our Holocene baseline, anchored by the 5.2 ka megadrought and the 18th century drought minimum, implies that such intensification would push Yangtze Basin rainfall toward the upper bounds of Holocene variability[34,41–43], with consequent heightened flood risk in the Yangtze River basin.

Several limitations point towards productive future work. The dominant source of uncertainty is palaeotemperature error (RMSE ≈ 2.6°C, driving ~25% of confidence interval width[20]), with regression residuals contributing a further ~10%. A further consideration is the assumption of quasi-steady-state epikarst hydrology implicit in the calibration. As described above, the 1760–1850 CE interval exhibits extreme drip rate variability (3.2–50.9 drips min^{-1}) that contrasts sharply with the tight, smooth PDF collapse at 5.2 ka (~1.7 drips min^{-1}), which indicates a quasi-steady low-flow state where the calibration remains valid. The kinetic proxy is thus most reliable as a precipitation indicator during sustained climate states — exactly the regime relevant to the megadrought that is the primary finding of this study. A further consequence of the two-stage regression architecture is its compressive effect on reconstructed precipitation extremes: the non-zero intercepts in both regression stages impose a physical floor on P even at near-zero drip rates, while the slope saturates at high drip rates. This produces near-symmetric precipitation anomalies (e.g. −35% at the 18th century drought minimum versus +16% at the post-1800 peak) from highly asymmetric underlying drip rate excursions (4.6 versus 38.7 drips min^{-1}), and means that the precipitation-space reduction at 5.2 ka corresponds to a >90% collapse in cave recharge (92% at native resolution; 84% in the 1-cm-smoothed reconstruction). Pairing the kinetic proxy with fluid-inclusion or clumped-isotope thermometry[44] would substantially tighten temperature constraints. Expanding the trace metal suite to include elements with contrasting dissociation rates (e.g. Zn, Cu, REE[15]) and incorporating stable metal isotope constraints (e.g. δ^{60}Ni; see Supplementary Methods 8) offer complementary validation pathways. Dissolved organic matter variability[16,45] represents a source of non-stationarity addressable through multi-biomarker approaches (Supplementary Methods 8). Broadly, the OMC dissociation framework is geochemically general: a global speleothem drip-rate network[3,6,46] would transform the spatial coverage of quantitative Holocene hydroclimate reconstructions. More fundamentally, because OMC dissociation kinetics are a property of aqueous metal–organic geochemistry rather than a site-specific phenomenon, the framework extends beyond speleothems to any carbonate or mineral archive recording trace metals from waters containing dissolved organic matter (Supplementary Methods 10), substantially improving model validation[36,47] and water security planning for monsoon-dependent societies.

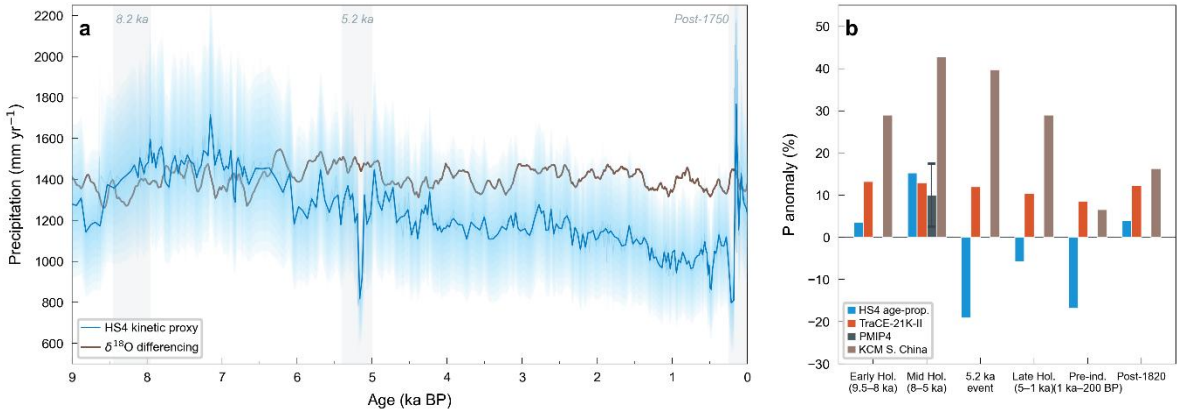


Figure 6 | Holocene precipitation reconstruction and model–data comparison for stalagmite HS4. **(a)** Annual precipitation reconstruction from the kinetic proxy (teal; median line with gradient-shaded IQR envelope from Monte Carlo simulation propagating drip rate posterior, regression parameter, residual, and palaeotemperature uncertainties; N = 10,000 draws per age; shown at 1-cm resolution (255 ages, primary) with native BayProX resolution (576 ages) as faint overlay). The $\delta^{18}O$ spatial differencing reconstruction[31] (brown) is shown for comparison. Shaded vertical bands mark the 8.2 ka event, the ~5.2 ka event, and the post-1750 CE interval. The reconstruction resolves mean early-Holocene rainfall of ~1,300 mm yr^{-1} (peak ~1,500 mm yr^{-1}), the 5.2 ka megadrought (~800 mm yr^{-1}, ~33% below Holocene mean), and the late-Holocene orbital decline. **(b)** Precipitation anomalies (% relative to Holocene mean) for six sub-periods, comparing the HS4 kinetic proxy (teal) with TraCE-21K-II (blue)[48], PMIP4 mid-Holocene ensemble mean[36] (charcoal, ± 1 s.d.), and KCM southern China[49] (brown). The 5.2 ka event window (5,200–5,100 yr BP) captures the event core, showing a ~33% negative anomaly in the HS4 reconstruction — a signal absent from all model simulations. KCM overestimates precipitation anomalies across all periods; PMIP4 captures the direction of mid-Holocene change but underestimates its amplitude.

Methods

Cave monitoring and sample preparation

Heshang Cave (N30°27′, E110°25′) was monitored from 2005 to 2015, with drip rate, dripwater chemistry, and surface P/T data collected following Hu et al.[18]. The HS4 stalagmite chronology was established by U/Th dating and annual lamina counting[12,31] (Extended Data Fig. 6). Approximately 10 mg of calcite powder per sample was dissolved in 2% (v/v) high-purity HNO_3, diluted to ~10 mL (Ca matrix ~400 ppm), and analysed by solution ICP-MS at the State Key Laboratory of Geological Processes and Mineral Resources, China University of Geosciences, Wuhan, using an Agilent 7500a instrument (plasma power 1550 W; nebuliser gas flow ~1.06 L min^{-1}; uptake rate 0.4 mL min^{-1}). Calibration used single-element reference standards (Inorganic Ventures) matrix-matched with high-purity Ca; ^{103}Rh (~10 ppb) served as internal standard. Blank solutions (2% HNO_3) were interspersed every ten samples. Signal acquisition comprised 20–30 s background and 60 s sample measurement (Agilent MassHunter); precision was better than 5% for Ca, Ni, and Co, verified against certified reference materials. Outliers were filtered as detailed in Supplementary Methods 3.

Kinetic proxy model and Bayesian inversion

The kinetic proxy model is derived fully in Supplementary Methods 1. Key input parameters were median monitored aqueous concentrations of Co, Ni, and Ca; experimental partition coefficients (K_p[17,26]); fast and inert fractions (λ_F = 0.001[15,16]; λ_I = 0.10–0.40[15]); and independently measured dissociation rates (k_d[15]). Distribution parameters (μ, σ) were optimised by least-squares fitting of 10-yr moving averages of reconstructed and observed HS4 drip rates against Yichang P/T records (1950–2001; Supplementary Table 1). Drip rate

probability density functions were computed via numerical inversion using BayProX[21]. Sensitivity to λ_F and $[X_{aq}]$ is explored in Supplementary Methods 3–4. Stochastic propagation of aqueous concentration uncertainty was investigated by marginalising drip rate PDFs over log-normal priors for Ca, Co, and Ni (Supplementary Methods 11). Paired monitoring data (n = 92, 2007–2016) show Ca is uncorrelated with both trace metals ($|r| < 0.1$), confirming that independent Monte Carlo sampling correctly represents the covariance structure. However, applying raw monitoring standard deviations (CV 6–27%) to the stochastic inversion inflated uncertainty envelopes by 17–24×, because each milled powder ICP-MS measurement integrates ~25 years of deposition (~270 independent water chemistry observations), reducing effective concentration CVs to < 2%. Fixed median concentrations were therefore used throughout. The model's dependence on the molar ratio $[TE]_{aq}/[Ca]_{aq}$ rather than absolute concentrations provides inherent robustness to secular changes in water chemistry, since $[Ca]_{aq}$ is stabilised by carbonate dissolution equilibrium on timescales much shorter than the integration window, and the dominant driver of concentration change — hydrological dilution — cancels through the ratio (Supplementary Methods 11). Python code is archived at Zenodo[50]. Development of the Dr Paleo web application and supporting stochastic modules used LLM-assisted code generation to improve accessibility (Claude, Anthropic); all outputs were thoroughly tested, reviewed and validated by the authors.

Precipitation reconstruction

Absolute precipitation was reconstructed by chained regression: (i) Heshang drip rate → Heshang P/T; (ii) Heshang P/T → Yichang P/T; (iii) P = (P/T)Yichang × T × 365.25, with T from Wang et al.[20]. Regression parameters and uncertainties are given in Supplementary Table 2. Monte Carlo propagation (N = 10,000 draws per age horizon) sampled log-normal drip rate posteriors, Gaussian regression residuals, and Gaussian temperature uncertainty (SD = 2.6°C), interpolated to the 73–8807 BP age grid of the temperature reconstruction. Anomalies are relative to the late Holocene mean (2.0–0.2 ka). The 5.2 ka event amplitude is the percentage departure from the mid-Holocene mean (6.5–5.5 ka). Pearson correlations with 30°N June insolation[21] used reconstructed precipitation medians; model comparisons employed published anomaly fields from TraCE-21ka[48], PMIP4[36], and KCM[49].

Recurrence quantification analysis

RQA[28] was applied to the full ensemble of 1,000 Monte Carlo realisations for both the drip rate and $\delta^{18}O$ proxy records. Time delay (τ) and embedding dimension (m) were estimated once from each proxy's full normalised median time series: τ via the first minimum of the average mutual information function, and m via Cao's method, bounded to $m \in [2, 5]$. Both proxies returned $\tau = 1$ and $m = 5$; these global parameters were applied uniformly across all windows and realisations. Per-window estimation of τ and m on 100-point segments is insufficiently stable for proxy data of this length and can introduce spurious variance into RQA measures; global estimation from the full series is more reproducible and defensible. The recurrence threshold was set by fixing the recurrence rate at RR = 0.05, following Kraemer et al., ensuring DET and TRANS are directly comparable across windows and realisations independent of signal amplitude. The Theiler window was $w = \tau \times (m - 1) = 4$, excluding autocorrelated neighbours along the line of identity. Determinism (DET) measures the fraction of recurrence points forming diagonal lines of length ≥ 2, quantifying signal regularity and predictability. Transitivity (TRANS) is the recurrence network clustering coefficient, quantifying the local geometrical density of the reconstructed phase space attractor: elevated TRANS indicates episodes where the system dwells within a restricted, densely revisited region of state space. RQA was computed in a sliding window of 100 points (step 5 points); ensemble medians and 5th/95th percentile envelopes were derived from the 1,000-realisation array. Gaussian smoothing (σ = 2 window steps) was applied to ensemble statistics for display. DET is persistently high (~0.75) in both records throughout, reflecting stable orbital-scale forcing. Positive TRANS excursions in the drip rate record — most prominently at ~5.2 ka — are interpreted as transient attractor constrictions during reduced-precipitation episodes and are

absent from the $\delta^{18}O$ record. A supplementary recurrence plot figure is given in Supplementary Methods 6.

Spectral and proxy-agreement analysis

Lomb–Scargle periodograms were computed for the detrended native-resolution drip rate (n = 585) and $\delta^{18}O$ (n = 1,223) time series on the best-estimate chronology, over frequencies corresponding to periods of 40–5,000 yr. False-alarm probability levels (1%, 5%, 10%) were estimated via the bootstrap method implemented in astropy. Cross-spectral coherence and phase were computed by Welch's method on both series interpolated to a regular 20-yr grid (segment length 256). To quantify time-varying proxy agreement, Z-scores of the drip rate and inverted $\delta^{18}O$ series (such that positive values indicate wetter conditions in both) were computed on the 20-yr common grid and multiplied pointwise; the resulting agreement metric was smoothed with a Gaussian kernel (σ = 5 grid points = 100 yr). Positive values indicate periods where both proxies record the same direction of hydrological change; negative values indicate disagreement (Extended Data Fig. 5).

Acknowledgements

Funded by EU Horizon 2020 Marie Skłodowska-Curie Actions (grant no. 691037; QUEST); Te Apārangi Royal Society of New Zealand (RIS-UOW1501); Ministry for Business, Innovation and Employment (UOWX2102); and a Rutherford Discovery Fellowship (RDF-UOW1601). The browser-based model interface (dr_app/) and stochastic concentration prior modules were developed with assistance from Claude (Anthropic, 2025). All scientific code (model.py, drip_rate_util.py, BayProX) and the kinetic model equations were authored by the research team.

Author contributions

A.H. conceived the study, developed the kinetic proxy model with B.G. and S.H., performed the recurrence quantification analysis with N.M., statistical tests, and wrote the manuscript. B.G. developed the core Python scripts (model.py, drip_rate_util.py), including the Bayesian inversion framework (BayProX[21]). S.H. performed the OMC dissociation experiments and contributed to proxy model development. J.P. contributed to data analysis, python code and software development. D.T.R. contributed to mathematical derivations and calculations. J.L. and C.H. provided the HS4 stalagmite samples, monitoring data, and ICP-MS analyses. B.R.S.F. contributed to interpretation and manuscript revision. N.M. contributed to the recurrence analysis methodology and interpretation. S.F.M.B. contributed to interpretation of karst processes, figures and manuscript revision. All authors discussed the results and commented on the manuscript.

Competing interests

The authors declare no competing interests.

Data availability

All data supporting the findings of this study are archived at Zenodo (https://doi.org/10.5281/zenodo.16392750) and are publicly available. The HS4 stalagmite trace metal, $\delta^{18}O$, and monitoring datasets are included in the repository as supplementary Excel files. Yichang meteorological data are available from the China Meteorological Administration. GPCP v2.3 precipitation data are available from https://psl.noaa.gov/data/gridded/data.gpcp.html. The 30°N June insolation data of Berger & Loutre[22] are publicly archived.

Code availability

The kinetic proxy forward model, Bayesian inversion code, and precipitation reconstruction scripts are available at GitHub (https://github.com/waikatosci/paleodriprates.git) and archived at Zenodo[50]. Key scripts include model.py (dissociation kinetics) and drip_rate_util.py (Bayesian inversion). The code requires Python 3.12 with numpy, pandas, matplotlib, scipy, and BayProX. A browser-based graphical interface (Dr Paleo) is available in the repositories (https://github.com/waikatosci/paleodriprates/tree/main/dr_app).

Extended Data Figure Legends

Extended Data Figure 1 | Holocene evolution of HS4 drip discharge in Smart & Friedrich hydrological classification space. Drip rate median and coefficient of variation (CV = σ/μ) computed in 250-yr bins and plotted in the hydrological classification framework of Smart & Friedrich (after Baker & Fairchild, 2012). Each circle represents one 250-yr bin, coloured by bin midpoint age; error bars show IQR (mean) and bootstrapped IQR (CV). Red star: whole-record summary (μ = 20.7 drips min^{-1}, CV = 0.21; error bars show IQR). Triangle: 5.2 ka event minimum (~7 drips min^{-1}), coloured by age. Green diamond: modern HS4 monitoring data (2005–2015; n = 112; μ = 16.0 drips min^{-1}, CV = 0.41). During stable climate intervals, the reconstruction occupies the low-CV Buffered overflow quadrant. The 5.2 ka aridity pulse resolves as a sharp excursion toward low mean drip rate and elevated CV, reflecting the abrupt transition into and out of the event.

Extended Data Figure 2 | Recurrence quantification analysis (RQA) and Holocene proxy probability density functions for HS4. (a) Ensemble RQA metrics for the $\delta^{18}O$ record: determinism (DET; grey) and transitivity (TRANS; dark green) with 5th–95th percentile uncertainty envelopes (see Methods for parameterisation). Shaded vertical bands mark the 8.2 ka event (blue), the end of the Green Sahara at ~5.2 ka (orange), and the post-1800 CE period (grey). (b) Normalised probability density functions for the $\delta^{18}O$ ensemble (blue colour map; y-axis inverted), with ensemble median (red) and 25th/75th percentile bounds (dashed red). (c) Ensemble RQA metrics for the kinetic-proxy drip rate series, same parameterisation as (a). DET is persistently high (~0.75) in both proxy records, reflecting stable orbital-scale forcing. TRANS in the drip rate record shows episodic positive excursions most prominently at ~5.2 ka (dashed vertical lines; dotted horizontal reference at TRANS = 0.5), absent from the $\delta^{18}O$ record, indicating transient attractor constrictions during low-drip episodes. (d) Normalised probability density functions for the drip rate ensemble (green colour map) with ensemble median and 25th/75th percentile bounds (black).

Extended Data Figure 3 | Drip rate probability density through three key Holocene events. Each column focuses on one event: (a) the 8.2 ka event (7,800–8,600 yr BP), (b) the 5.2 ka event (4,800–5,600 yr BP), and (c) the pre- and post-industrial transition (~1,680–2,010 CE). Posterior probability density of the HS4 kinetic drip rate reconstruction (GnBu colourmap; Gaussian kernel from native-resolution percentiles, normalised per time step) with median (grey) and IQR fill. The raw $\delta^{18}O$ record (right axis, inverted) is overlaid. At 8.2 ka, the Liu et al. (2013) high-resolution (~annual) $\delta^{18}O$ record (brown; published ages) is additionally shown. Panel (c) includes historical event markers and a post-1850 decline trend line.

Extended Data Figure 4 | Fine-grained statistical analysis of the 8.2 ka event on the best-estimate chronology. (a) Detrended drip rate median (pc50) through the 7,500–9,500 yr BP analysis range, with event core (blue shading), linear orbital trend (dotted), and flanking windows. (b) Multi-scale rolling-window detrended median (50, 100, 150, 200 yr windows) with early-Holocene baseline reference (dotted). (c) Rolling Mann–Whitney U p-values for each window size against the baseline (8,800–9,300 yr BP); dashed and dotted lines mark p = 0.05 and p = 0.01. (d) Rolling rank-biserial effect size; dotted lines mark |r| = 0.3 (moderate effect). A local flanking-baseline test (event core 8,100–8,250 yr BP versus combined pre- and post-event flanks) yields no statistically significant difference.

Extended Data Figure 5 | Spectral analysis of drip rate and $\delta^{18}O$ variability. (a) Lomb–Scargle periodogram of the detrended native-resolution drip rate record (n = 585; median spacing 14.6 yr). Dashed lines show 1% and 5% false-alarm probability levels. Significant peaks are annotated. (b) Lomb–Scargle periodogram of the detrended $\delta^{18}O$ record (n = 1,223; median spacing 3.3 yr). (c) Cross-spectral coherence (blue; left axis) and phase (red scatter; right axis) computed by Welch's method on a 20-yr interpolated grid. The two proxies share no significant periodicities at the 5% level, confirming that the kinetic proxy records infiltration–recharge dynamics spectrally independent from the moisture-source signal preserved in $\delta^{18}O$.

Extended Data Figure 6 | HS4 age–depth chronology. (a) Full age–depth model showing 31 U–Th tie points (red circles; 2σ error bars) and 11 densely sampled 8.2 ka zone tie points (orange squares) against the interpolated 1-yr resolution model (blue curve). Inset: growth rate (cm kyr^{-1}) derived from the monotonic interpolation. Orange shading marks the 8.2 ka dating zone (228–240 cm). (b) Detail of the 8.2 ka zone showing age reversals in the raw U–Th dates with individual age ± 2σ labels (dashed connectors). The interpolated model (blue) threads monotonically through the reversals, which reflect the inherent difficulty of resolving sub-centennial chronology through this interval. All figure scripts in this study use this chronology for depth-to-age conversion.

References

1. FAO. *Asia and the Pacific Regional Overview of Food Security and Nutrition 2020*. (2021).
2. Wang, Y. *et al.* Millennial- and orbital-scale changes in the East Asian monsoon over the past 224,000 years. *Nature* **451**, 1090–1093 (2008).
3. Wang, P. X. *et al.* The global monsoon across timescales: coherent variability of regional monsoons. *Climate of the Past* **10**, 2007–2052 (2014).
4. Azharuddin, S. *et al.* Multidecadal hydroclimate responses to volcanic forcing in the Mid-Holocene. *Communications Earth & Environment* **6**, 101 (2025).
5. Moon, S. *et al.* Anthropogenic warming induced intensification of summer monsoon frontal precipitation over East Asia. *Sci. Adv.* **9**, eadh4195 (2023).
6. Fairchild, I. J. & Baker, A. *Speleothem Science: From Process to Past Environments*. (Wiley, 2012). doi:10.1002/9781444361094.
7. Yu, T., Chen, W., Huang, P., Huang, G. & Yang, X. Weakened influence of ENSO on the East Asian summer monsoon since the early 2000s. *npj Clim Atmos Sci* **8**, 114 (2025).
8. Ashok, K., Guan, Z. & Yamagata, T. Impact of the Indian Ocean dipole on the relationship between the Indian monsoon rainfall and ENSO. *Geophysical Research Letters* **28**, 4499–4502 (2001).
9. Cheng, H. *et al.* The Asian monsoon over the past 640,000 years and ice age terminations. *Nature* **534**, 640–646 (2016).
10. Lachniet, M. S. Climatic and environmental controls on speleothem oxygen-isotope values. *Quaternary Science Reviews* **28**, 412–432 (2009).
11. Deininger, M., Fohlmeister, J., Scholz, D. & Mangini, A. Isotope disequilibrium effects: The influence of evaporation and ventilation effects on the carbon and oxygen isotope composition of speleothems – A model approach. *Geochimica et Cosmochimica Acta* **96**, 57–79 (2012).
12. Liu, Y.-H. *et al.* Links between the East Asian monsoon and North Atlantic climate during the 8,200 year event. *Nature Geoscience* **6**, 117–120 (2013).
13. Owen, R. A. *et al.* Calcium isotopes in caves as a proxy for aridity: Modern calibration and application to the 8.2 kyr event. *Earth and Planetary Science Letters* **443**, 129–138 (2016).
14. Treble, P. C. *et al.* Impacts of cave air ventilation and in-cave prior calcite precipitation on Golgotha Cave dripwater chemistry, southwest Australia. *Quaternary Science Reviews* **127**, 61–72 (2015).

15. Höpker, S. N., Breitenbach, S. F. M., Grainger, M., Stirling, C. H. & Hartland, A. Characterising the decay of organic metal complexes in speleothem-forming cave waters. *Geochimica et Cosmochimica Acta* **373**, 98–108 (2024).
16. Hartland, A. & Zitoun, R. Transition metal availability to speleothems controlled by organic binding ligands. *Geochemical Perspectives Letters* 22–25 (2018) doi:10.7185/geochemlet.1824.
17. Lindeman, I., Hansen, M., Scholz, D., Breitenbach, S. F. M. & Hartland, A. Effects of organic matter complexation on partitioning of transition metals into calcite: Cave-analogue crystal growth experiments. *Geochimica et Cosmochimica Acta* **317**, 118–137 (2022).
18. Hu, C., Henderson, G., Huang, J., Chen, Z. & Johnson, K. Report of a three-year monitoring programme at Heshang Cave, Central China. *International Journal of Speleology* **37**, 143–151 (2008).
19. Hu, C. *et al.* Quantification of Holocene Asian monsoon rainfall from spatially separated cave records. *Earth and Planetary Science Letters* **266**, 221–232 (2008).
20. Wang, C. *et al.* Holocene temperature and hydrological changes reconstructed by bacterial 3-hydroxy fatty acids in a stalagmite from central China. *Quaternary Science Reviews* **192**, 97–105 (2018).
21. Goswami, B. *et al.* Estimation of sedimentary proxy records together with associated uncertainty. *Nonlinear Processes in Geophysics* **21**, 1093–1111 (2014).
22. Berger, A. & Loutre, M. F. Insolation values for the climate of the last 10 million years. *Quaternary Science Reviews* **10**, 297–317 (1991).
23. deMenocal, P. *et al.* Abrupt onset and termination of the African Humid Period: *Quaternary Science Reviews* **19**, 347–361 (2000).
24. Griffiths, M. L. *et al.* End of Green Sahara amplified mid- to late Holocene megadroughts in mainland Southeast Asia. *Nature Communications* **11**, 4204 (2020).
25. Shanahan, T. M. *et al.* The time-transgressive termination of the African Humid Period. *Nature Geoscience* **8**, 140–144 (2015).
26. Lakshtanov, L. Z. & Stipp, S. L. S. Experimental study of nickel(II) interaction with calcite: Adsorption and coprecipitation. *Geochimica et Cosmochimica Acta* **71**, 3686–3697 (2007).
27. Huang, C., Zeng, T., Ye, F. & Wei, G. Solar-forcing-induced spatial synchronisation of the East Asian summer monsoon on centennial timescales. *Palaeogeography, Palaeoclimatology, Palaeoecology* **514**, 536–549 (2019).
28. Marwan, N., Carmenromano, M., Thiel, M. & Kurths, J. Recurrence plots for the analysis of complex systems. *Physics Reports* **438**, 237–329 (2007).
29. Lin, K.-H. E., Wang, P. K., Pai, P.-L., Lin, Y.-S. & Wang, C.-W. Historical droughts in the Qing dynasty (1644–1911) of China. *Clim. Past* **16**, 911–931 (2020).
30. Hang, X. *et al.* Temporal and Spatial Effects of Extreme Drought Events on Human Epidemics over Ancient China in 1784–1787 CE. *Environ Health* **24**, 8 (2025).
31. Hu, C. *et al.* Quantification of Holocene Asian monsoon rainfall from spatially separated cave records. *Earth and Planetary Science Letters* **266**, 221–232 (2008).
32. Haug, G. H., Hughen, K. A., Sigman, D. M., Peterson, L. C. & Röhl, U. Southward Migration of the Intertropical Convergence Zone Through the Holocene. *Science* **293**, 1304–1308 (2001).
33. Cheng, J. *et al.* Vegetation feedback causes delayed ecosystem response to East Asian Summer Monsoon Rainfall during the Holocene. *Nature Communications* **12**, 1843 (2021).
34. Wang, Y. *et al.* A quantitative reconstruction of Holocene annual precipitation in the marginal zone of the East Asian summer monsoon. *Palaeogeography, Palaeoclimatology, Palaeoecology* **596**, 110968 (2022).
35. Cai, Y. *et al.* Holocene variability of East Asian summer monsoon as viewed from the speleothem δ 18 O records in central China. *Earth and Planetary Science Letters* **558**, 116758 (2021).

36. Brierley, C. M. *et al.* Large-scale features and evaluation of the PMIP4-CMIP6 *midHolocene* simulations. *Clim. Past* **16**, 1847–1872 (2020).
37. Du, Y., Brown, J. R., Menviel, L., Saini, H. & Drysdale, R. N. The Impacts of an AMOC Slowdown on Southern Hemisphere and Australian Climates at 8.2 ka in ACCESS-ESM1.5 Model. *JGR Atmospheres* **130**, e2024JD042432 (2025).
38. Parker, S. E. & Harrison, S. P. The timing, duration and magnitude of the 8.2 ka event in global speleothem records. *Scientific Reports* **12**, 10542 (2022).
39. Lang, Y. *et al.* Mechanisms and quantification: How anthropogenic aerosols weaken the East Asian summer monsoon. *npj Climate and Atmospheric Science* **8**, 13 (2025).
40. Lu, F. *et al.* Tipping point-induced abrupt shifts in East Asian hydroclimate since the Last Glacial Maximum. *Nat Commun* **16**, 477 (2025).
41. Katzenberger, A. & Levermann, A. Consistent increase in East Asian Summer Monsoon rainfall and its variability under climate change over China in CMIP6. *Earth System Dynamics* **15**, 1137–1151 (2024).
42. Zhang, C. *et al.* Projecting multi-attribute flood regime changes for the Yangtze River basin. *Journal of Hydrology* **617**, 128846 (2023).
43. IPCC. *Global Warming of 1.5°C*. (2018).
44. Wassenburg, J. A. *et al.* Penultimate deglaciation Asian monsoon response to North Atlantic circulation collapse. *Nat. Geosci.* **14**, 937–941 (2021).
45. Hartland, A. *et al.* From soil to cave: Transport of trace metals by natural organic matter in karst dripwaters. *Chemical Geology* **304–305**, 68–82 (2012).
46. Kaushal, N. *et al.* SISALv3: a global speleothem stable isotope and trace element database. *Earth Syst. Sci. Data* **16**, 1933–1963 (2024).
47. Xue, D. *et al.* Robust projection of East Asian summer monsoon rainfall based on dynamical modes of variability. *Nat Commun* **14**, 3856 (2023).
48. Liu, Z. *et al.* Transient Simulation of Last Deglaciation with a New Mechanism for Bølling-Allerød Warming. *Science* **325**, 310–314 (2009).
49. Park, W. *et al.* Tropical Pacific Climate and Its Response to Global Warming in the Kiel Climate Model. *Journal of Climate* **22**, 71–92 (2009).
50. Hartland, A., Goswami, B. & Park, J. waikatosci/paleodriprates: paleo_drip. Zenodo https://doi.org/10.5281/ZENODO.18690925 (2026).

Supplementary Files

This is a list of supplementary files associated with this preprint. Click to download.

- SuppHartlandfin.docx